Aalto University

OPEN ACCESS

This is an electronic reprint of the original article.
This reprint may differ from the original in pagination and typographic detail.

Virk, Usman; Nguyen, Sinh; Haneda, Katsuyuki; Wagen, Jean-Frederic

On-Site Permittivity Estimation at 60 GHz through Reflecting Surface Identification in the Point Cloud

Published in:
IEEE Transactions on Antennas and Propagation

DOI:
10.1109/TAP.2018.2829798

Published: 01/07/2018

Document Version
Peer-reviewed accepted author manuscript, also known as Final accepted manuscript or Post-print

Please cite the original version:
Virk, U., Nguyen, S., Haneda, K., & Wagen, J.-F. (2018). On-Site Permittivity Estimation at 60 GHz through Reflecting Surface Identification in the Point Cloud. *IEEE Transactions on Antennas and Propagation*, *66*(7), 3599-3609. https://doi.org/10.1109/TAP.2018.2829798

This material is protected by copyright and other intellectual property rights, and duplication or sale of all or part of any of the repository collections is not permitted, except that material may be duplicated by you for your research use or educational purposes in electronic or print form. You must obtain permission for any other use. Electronic or print copies may not be offered, whether for sale or otherwise to anyone who is not an authorised user.

This article has been accepted for publication in a future issue of this journal, but has not been fully edited. Content may change prior to final publication. Citation information: DOI 10.1109/TAP.2018.2829798, IEEE Transactions on Antennas and Propagation

On-Site Permittivity Estimation at 60 GHz through Reflecting Surface Identification in the Point Cloud

Usman Tahir Virk, Sinh Le Hong Nguyen, *Member, IEEE*, Katsuyuki Haneda, *Member, IEEE* and Jean-Frederic Wagen, *Member, IEEE*

***Abstract*—Accurate site-specific radio propagation simulations provide an important basis for cellular coverage analysis. The quality of these simulations relies on the accuracy of environmental description and electrical properties of constituent materials. This paper presents a novel method of on-site permittivity estimation. The method utilizes an accurate geometrical database of the environment for identifying flat and smooth surfaces producing reflections. The method exploits a limited number of on-site channel sounding to extract reflected multipaths, and compare them with ray-tracing based on the environmental database. The permittivity of the identified reflecting surfaces is estimated by solving an inverse reflection problem. The method was experimentally tested with a limited radio channel measurements at 60 GHz in a large empty office room. The identified reflecting surfaces are classified according to their mean permittivity estimates, showing their consistency with physical material evidence and the permittivity database in the ITU recommendation. The estimated permittivity values are visualized as a three-dimensional map, giving an intuitive understanding of materials constituting the environment. Our work demonstrates on-site permittivity estimation and material classification without the need for isolated measurements of composite materials in an anechoic chamber or in-situ measurements of built environments.**

***Index Terms*—Millimeter wave, point cloud, ray-tracing, surface identification, permittivity, visualization.**

I. Introduction

WITHIN the last decade, wireless data traffic has been increasing at a phenomenal rate. As recent statistics indicate [1], [2], there will be a 10,000-fold increase in wireless data traffic over the next 20 years, mainly driven by applications requiring large bandwidth. Dealing with this magnitudinous demand for high data rates with reliable communication will require enabling technologies with suitable radio spectrum. A viable solution may be fifth generation (5G) wireless networks operating in a wide frequency range including the millimeter wave spectrum. For this purpose, 5G standards have been developed by the telecommunication industry in alliance with the scientific community. Deployment and successful role out of 5G wireless systems requires realistic site-specific coverage estimates.

Radio channel measurements serve as ground-truth for radio coverage simulations. However, measurements are usually cumbersome and constrained to quality equipment and other resources. In addition, the coverage study requires a huge sample size of channel parameters to resemble the reality, which is not always available from measurements subject to practical restrictions. Therefore, site-specific radio wave propagation simulations calibrated with a limited number of measurements play a key role in the coverage analysis. Various techniques to simulate radio wave propagation are available, either based on full-wave electromagnetic methods such as Finite-difference time-domain (FDTD) [3]–[6] and references therein, or the optical approximation of radio wave propagation known as ray-based models, e.g., [7]–[13] and references therein among others.

Building structures and materials strongly influence radio wave propagation [14]–[20], and therefore the service coverage. The site-specific radio propagation simulations always require an authentic source for material electrical properties irrespective of the implemented technique. The reflection loss associated with specular multipath can be evaluated by employing the Fresnel reflection coefficients, provided that the permittivity of the reflecting surface is known. The modus operandi to obtain the permittivity of a given material sample is through isolated material measurements, which is widely reported in the literature [21]–[28]. However, this approach does not easily allow the determination of the permittivity of built-in composite materials for varying environments. To cope with this issue, in-situ measurements within the environment are conducted for specific building structures to evaluate the reflection loss, as presented in [16], [18], [19], [29]–[31]. This reflection loss is then used to determine the permittivity of the reflecting surface by regression analysis, as reported in [15], [17], [20], [32]–[35]. Although this process provides a reasonable estimate of permittivity for the built-in reflecting surface of composite materials, it is an exceedingly difficult task to identify and cover all surfaces comprehensively in a given environment.

We, therefore in this article, propose a novel method to estimate permittivities of composite materials in built environments. We exploit radio channel sounding campaign where it is possible to obtain a large number of multipaths estimates based on a limited number of measurements of the radio

Manuscript received June 28, 2017; revised January 17, 2018; accepted April 14, 2018. Date of publication Month XX, 2018; date of current version Month XX, 2018. This work is financially supported by Academy of Finland through WiFiUS project: “Device-to-Device communication for millimeter wave”, decision number 284709.

U.T. Virk, and K. Haneda are with the Department of Electronics and Nanoengineering, School of Electrical Engineering, Aalto University, FI-00076 Espoo, Finland (e-mail: usman.virk@aalto.fi, katsuyuki.haneda@aalto.fi).

S. L. H. Nguyen was with the Department of Electronics and Nanoengineering, School of Electrical Engineering, Aalto University, FI-00076 Espoo, Finland. He is now with Ericsson Research, 41756 Gothenburg, Sweden (e-mail: sinh.l.nguyen@ericsson.com).

J-F. Wagen is with the University of Applied Sciences and Arts of Western Switzerland, HES-SO, Fribourg, EIA-FR Perolle-80, CH-1705 Fribourg, Switzerland (e-mail: jean-frederic.wagen@hefr.ch).

0018-926X (c) 2018 IEEE. Personal use is permitted, but republication/redistribution requires IEEE permission. See http://www.ieee.org/publications_standards/publications/rights/index.html for more information.

This article has been accepted for publication in a future issue of this journal, but has not been fully edited. Content may change prior to final publication. Citation information: DOI 10.1109/TAP.2018.2829798, IEEE Transactions on Antennas and Propagation

environments. We utilize these multipaths for comprehensive characterization of materials in a physical environment by solving an inverse reflection problem. The inverse problem fuses the measured multipaths with the physical environment through: 1) ray-tracing using accurate three-dimensional (3D) description of the environment, 2) reflecting surface identification, and 3) permittivity estimation. Our goal is to demonstrate that a small number of channel sounding allows comprehensive estimates of permittivity in an environment, giving rise to a 3D permittivity map. Hence, thorough measurements of each composite material in a built-environment are not required.

The main contributions of this article are as follows.

1. Detailed analytical formulation of the novel method for on-site permittivity estimation in built environments, attributing multipaths from limited channel sounding to the environment.
2. Demonstrated feasibility of the proposed method in a large empty office, creating a 3D permittivity map of the environment at 60 GHz radio frequency.
3. Demonstrated soundness of the estimated permittivities by showing their consistency with those reported in the ITU recommendation.

The rest of the paper is organized in four sections: Section II formulates the method analytically and identify the necessary inputs to the method. It also discusses the favorable conditions for adequate performance of the proposed method in terms of reliable estimates of material permittivities. Section III presents the exemplary radio channel measurements at 60 GHz in a large empty office and multipath extraction for demonstrating the proposed method. Section IV provides the 3D permittivity map of the environment, where the identified reflecting surfaces corresponding to the measured multipaths are colored with the permittivity estimates. Their validity is discussed through comparison with physical material evidence and the ITU-R document. Finally, the paper is concluded in Section V.

II. On-Site Permittivity Estimation

A. Conditions

Before describing the method itself, we define two conditions where the method works most suitably to estimate the permittivity of materials in the environment. These are the availability of 1) accurate geometrical database of the environment and 2) rich single-bounce specular reflections.

1) Accurate geometrical database of the environment: Availability of accurate geometrical database of the environment of interest is a prerequisite for obtaining sound matching of multipaths from measurements and ray-tracing. When publicly available geometrical representation of the environment is used, many measured multipaths fail to find their ray-traced counterparts because of the inherent inaccuracies and irregularities in the geometrical representation of the environment. These inaccuracies may include missing objects that are electrically large-enough for producing reflections, such as signboards in outdoors and bookshelves in indoors. This is more prominent at higher radio frequencies as physically small and flat objects can be electrically large-enough to produce reflections. The accurate geometrical database can be acquired through modern laser scanning equipment. It is called a point cloud and is a set of points in the Cartesian coordinate system. We assume in this paper that the point cloud is available for the site of interest in which the comprehensive permittivity estimates are required.

2) Single-bounce specular reflections: The second condition that makes the proposed method function properly is the abundance of single-bounce specular reflections. As long as a sufficient number of single-bounce specular reflections are available to cover a given environment, the proposed method performs robustly regardless of the frequency. The specular multipaths reflects off flat and electrically large surfaces, particularly, when their first Fresnel zones fall well within the surfaces. The width of the first Fresnel zone is given by $W_{\mathrm{F}} = 2\sqrt{\frac{\lambda d_1 d_2}{d_1+d_2}}$, with λ as the wavelength, and d_1 and d_2 as the propagation distances at any point on a straight line between the link ends, indicating that it decreases with increasing radio frequency or decreasing propagation distance. Reflections are therefore observed more frequently from flat surfaces when they are close to the transmitting (Tx) and receiving (Rx) antennas, and/or the radio frequency is higher. This condition physically justifies the use of image sources in conjunction with the Friis' equation. Generally, for multi-bounce specular reflections, the Friis' equation is

$$\mathrm{PG} = G_{\mathrm{Tx}} G_{\mathrm{Rx}} \left(\frac{\lambda}{4\pi d_{\mathrm{r}}}\right)^2 \prod_{i=1}^{I} |\Gamma_i|^2, \tag{1}$$

where PG is the path gain, G_{Tx} and G_{Rx} are the Tx and Rx antenna gain, respectively, λ is wavelength of the propagating wave, d_{r} is the path length, and $|\Gamma_i|$ is the Fresnel reflection coefficient of the i-th reflecting surface. Depending on the orientation of the reflecting surface, $|\Gamma|$ can be categorized into either a parallel or perpendicular polarization [36], denoted by the subscripts $\|$ and $\perp$, respectively. By using (1), it is possible to evaluate $|\Gamma|$ empirically from the measured multipaths and hence inverse reflection problem can be solved to estimate the permittivity of the reflecting surface.

By considering a fine delay resolution in measurements, it is possible to isolate single-bounce specular reflections that provide estimates of $|\Gamma|$ in a most straightforward manner. Higher-order specular reflections can also be used to estimate the same for each interacting surface. When considering a multipath that interacts with surfaces $i-$times, $|\Gamma|$ of $i-1$ surfaces must be known in order to obtain the $|\Gamma|$ for a surface of interest. In this case, uncertainty of $|\Gamma|$ estimates from $i-1$ surfaces accumulates and hence the permittivity estimates are less accurate compared to the case of single-bounce paths. Therefore, we restrict the specular paths only to single-order to obtain most accurate permittivity estimates. Excluding multiple-bounce paths from the measurements would limit the total number of available paths for permittivity estimates. However, we show in the next section that performing several line-of-sight channel sounding with short Tx-Rx separation distances suffices for a comprehensive characterization of permittivity in a large empty office.

0018-926X (c) 2018 IEEE. Personal use is permitted, but republication/redistribution requires IEEE permission. See http://www.ieee.org/publications_standards/publications/rights/index.html for more information.

This article has been accepted for publication in a future issue of this journal, but has not been fully edited. Content may change prior to final publication. Citation information: DOI 10.1109/TAP.2018.2829798, IEEE Transactions on Antennas and Propagation

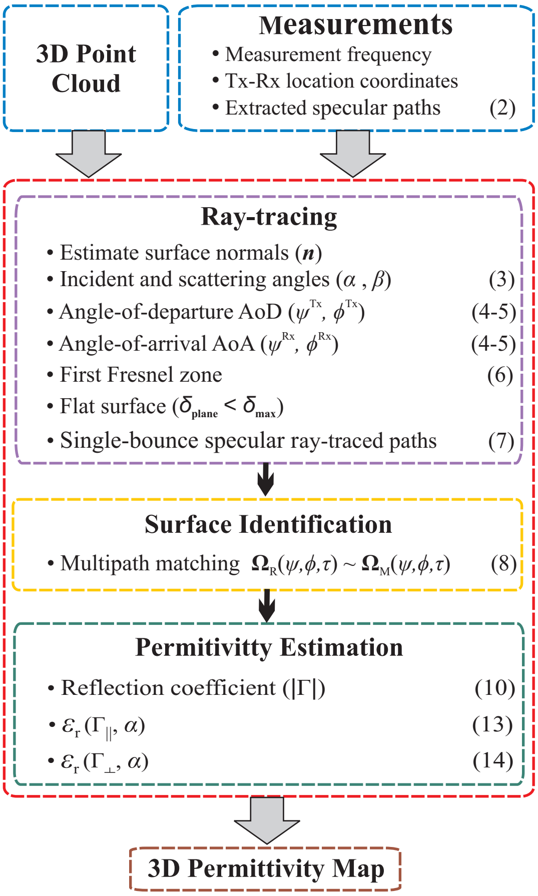

Fig. 1. Flowchart for the generation of permittivity map.

B. Method

The method requires three inputs: 1) accurate physical structural data of the environment of interest, in the form of point cloud in this paper 2) specifications of the channel sounding, e.g., the radio frequency and location coordinates of the Tx and Rx antennas, and finally 3) a set of multipaths extracted from the channel sounding data for each Tx-Rx link. The set of measured multipaths ranging from $1 \leq n \leq N_l$ in the Tx-Rx links varying between $1 \leq l \leq L$ are defined by

$$\boldsymbol{\Omega}_{\mathrm{M}}^{(l)} = \left\{\boldsymbol{\rho}_n, \tau_n, \psi_n^{\mathrm{Tx}}, \phi_n^{\mathrm{Tx}}, \psi_n^{\mathrm{Rx}}, \phi_n^{\mathrm{Rx}}\right\}_{n=1}^{N_l}, \tag{2}$$

where, for the n-th multipath in the l-th Tx-Rx link, $\boldsymbol{\rho}_n \in \mathbb{C}^{2\times 2}$ is the polarimetric path gain matrix, τ_n is the propagation delay, ψ_n^{Tx} and ϕ_n^{Tx} are the elevation and azimuth angles-of-departure (AoD) at the Tx, and ψ_n^{Rx} and ϕ_n^{Rx} are the elevation and azimuth angle-of-arrival (AoA) at the Rx. It must be noted that the available parameters in (2) depends on channel sounder configuration. A wideband channel sounder with proper synchronization between the Tx and Rx sides is required to have τ, while angular estimates may come from antenna array measurements or directional antenna scanning. Our method works even when some parameters in (2) are not available, as will be demonstrated in Section IV.

The method is designed in three main steps, namely: 1) ray-tracing, 2) multipath matching and surface identification and 3) permittivity estimation. The flowchart in Fig. 1 illustrates the overall estimation process with different steps referred by corresponding equations that are described in the following.

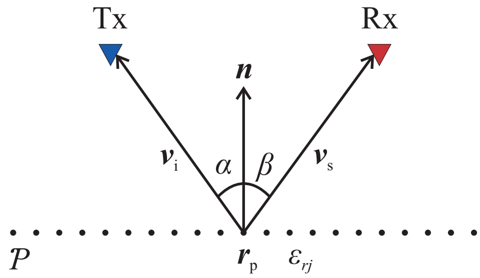

Fig. 2. Vectorial representation of ray-tracing in point cloud.

1) Ray-tracing: The first step exploits ray-tracing to identify multipath trajectories from the Tx to the Rx antenna. The trajectories are defined on the global coordinate systems, while the interactions of rays with the antennas and the reflecting surfaces are specified with respect to the local coordinates of the surface. The origin of the global coordinate system is defined within the point cloud description of the environment.

The ray-tracing evaluates the incident and the outgoing angles, α and β of a ray, respectively at each point $\boldsymbol{r}_{\mathrm{p}}$ in the point cloud on a local coordinate system. This requires the normal vector, or simply the *normal*, to a local surface formed around a particular point and vectors of the incident and outgoing rays. The normal at each point is estimated by fitting a local plane with eight of its neighboring points, similar to the method described in [37]. For this study, eight neighboring points are found to work best with the available density of the point cloud and to correctly identify the local surfaces and corresponding normals. The normal, the ray vectors and a point of interest is represented in Fig. 2. The incident and the outgoing ray vectors on each point in the point cloud are calculated by $\boldsymbol{v}_{\mathrm{i}} = \boldsymbol{r}_{\mathrm{Tx}} - \boldsymbol{r}_{\mathrm{p}}$ and $\boldsymbol{v}_{\mathrm{s}} = \boldsymbol{r}_{\mathrm{Rx}} - \boldsymbol{r}_{\mathrm{p}}$ where $\boldsymbol{r}_{\mathrm{Tx}}$ and $\boldsymbol{r}_{\mathrm{Rx}}$ are the position vectors for the Tx and Rx antenna locations, respectively. With these vectors and the normals $\boldsymbol{n}$, the corresponding incident α and outgoing β angles are obtained through,

$$\alpha, \beta = \arccos\left(\frac{\boldsymbol{v}_k \cdot \boldsymbol{n}}{|\boldsymbol{v}_k||\boldsymbol{n}|}\right) \qquad (k = \mathrm{i}, \mathrm{s}). \tag{3}$$

On the global coordinate system, the AoA and AoD can be obtained for the azimuth and elevation domains using

$$\psi = \arccos\left(\frac{\boldsymbol{v}_k \cdot \boldsymbol{v}_{\mathrm{p},k}}{|\boldsymbol{v}_k||\boldsymbol{v}_{\mathrm{p},k}|}\right) \qquad (k = \mathrm{i}, \mathrm{s}), \tag{4}$$

$$\phi = \arccos\left(\frac{\boldsymbol{v}_{\mathrm{p},k} \cdot \boldsymbol{u}_x}{|\boldsymbol{v}_{\mathrm{p},k}||\boldsymbol{u}_x|}\right) \qquad (k = \mathrm{i}, \mathrm{s}), \tag{5}$$

where $\boldsymbol{u}_x = [1\ 0\ 0]$ is a unit vector on the x-axis; $\boldsymbol{v}_{\mathrm{p},k} = \boldsymbol{v}_k - \left(\frac{\boldsymbol{v}_k \cdot \boldsymbol{u}_z}{|\boldsymbol{v}_k||\boldsymbol{u}_z|}\right)\boldsymbol{u}_z$ refers to the projection of the incidence or the outgoing vector $\boldsymbol{v}_k$ onto the x-y plane, with $\boldsymbol{u}_z = [0\ 0\ 1]$ being the unit vector along the z-axis.

For ray-traced specular paths, the Snell's law of reflection holds when incident angle α is equal to the reflection angle β. In case of a sparse point cloud, a situation may arise when the actual reflection point is left undocumented and it is not

0018-926X (c) 2018 IEEE. Personal use is permitted, but republication/redistribution requires IEEE permission. See http://www.ieee.org/publications_standards/publications/rights/index.html for more information.

possible to match the measured path with the corresponding ray-traced path. To solve this problem, a suitable threshold margin $\gamma_{\rm th}$ is introduced that represents the acceptable difference between α and β depending on the density of the given point cloud. As the sparsity of the point cloud increases, a relatively higher value of $\gamma_{\rm th}$ is needed to compensate for the missing reflection points. The specular reflections condition is applied to the set of single-bounce ray-traced paths fulfilling $|\alpha_{n'} - \beta_{n'}| \leq \gamma_{\rm th}$, where n' refers to the index of a ray-traced specular path. In addition to satisfying the Snell's law, the ray-traced paths must also originate from a large-enough flat surfaces. It has been demonstrated in [38] that at least first Fresnel reflection zone is required for accurately modeling the specular reflection in a point cloud. Therefore, the points in the point cloud falling into the first Fresnel zone of a reflecting surface are of our interest. For an n'-th ray-traced specular path, indices q of these points are found, according to the image theory, as

$$\begin{aligned} \hat{q} &= \arg_{q}\left\{|\tau_{\rm p}(q) - \tau_{n'}| \leq \frac{\lambda}{2}\right\}, \\ \tau_{\rm p}(q) &= \left\|\frac{\boldsymbol{r}_{\rm img}(q) - \boldsymbol{r}_{\rm Tx}(q)}{c}\right\|, \end{aligned} \tag{6}$$

where $\tau_{\rm p}$ refers to the delay of a ray-traced path between the Tx antenna and the image source of the Rx with position vectors $\boldsymbol{r}_{\rm Tx}$ and $\boldsymbol{r}_{\rm img}$, respectively and c being the speed of light in free space.

Finally in order to select a flat reflecting surface, we calculate the roughness depth $\delta_{\rm plane}$ (root-mean-squared (rms) height) of the identified first Fresnel zone. A surface is considered as flat and responsible for specular contribution, only if it satisfies the flatness criteria, $\delta_{\rm plane} < \delta_{\rm max}$, where $\delta_{\rm max}$ is a maximum predefined roughness depth. Theoretically, $\delta_{\rm max}$ must fulfill the Rayleigh smoothness criteria[1]. This implies that the selection of $\delta_{\rm max}$ depends on the radio frequency and the point cloud density. With a too sparse point cloud to be able to form a valid surface, it is difficult to estimate the true rms height of the surface profile. The set of single-bounce specular-reflected ray-traced paths are now described, partly in the same manner as measured multipaths (2), by

$$\boldsymbol{\Omega}_{\rm R}^{(l)} = \left\{\alpha_{n'}, \beta_{n'}, \tau_{n'}, \psi_{n'}^{\rm Tx}, \phi_{n'}^{\rm Tx}, \psi_{n'}^{\rm Rx}, \phi_{n'}^{\rm Rx}\right\}_{n'=1}^{N_l'}, \tag{7}$$

where α and β are the incident and outgoing angles of n'-th path, respectively. The total number of ray-traced paths for the l-th link is defined by N_l'.

2) Specular Multipath Matching and Reflecting Surface Identification: Reflecting surface identification in the point cloud is performed by matching specular multipaths from measurements and ray-tracing under uncertainties related to the density of the point cloud, estimates of multipath parameters and Tx-Rx locations. These uncertainties are represented by threshold margins $\psi_{\rm th}$ for the elevation AoD at Tx and Rx, $\phi_{\rm th}$ for the azimuth AoD at Tx and Rx, and τ_{th} for the propagation delays of paths. These threshold margins specify the minimum differences between measured and ray-traced paths such that they correspond to each other and hence are associated uniquely to the reflecting surfaces. For specular multipath matching, we require AoA, AoD and delay of the multipath. An index of a path from the ray-tracing $\hat{n}'$ that has the closest parameters to the n-th measured path is found by

$$\begin{aligned} \hat{n}' = \arg_{n'}\Big\{&|\tau_n - \tau_{n'}| \leq \tau_{\rm th}, |\psi_n^x - \psi_{n'}^x| \leq \psi_{\rm th}^x, \\ &|\phi_n^x - \phi_{n'}^x| \leq \phi_{\rm th}^x\Big\} \quad (x = {\rm Tx}, {\rm Rx}). \end{aligned} \tag{8}$$

This is repeated for all the measured paths and the optimal values for threshold margins $\psi_{\rm th}$, $\phi_{\rm th}$ and $\tau_{\rm th}$ are chosen heuristically. In general, reflecting surfaces in a propagation environment have different orientations, i.e., vertical, horizontal or slanted. Hence, all the identified surfaces at this stage are further attributed to their orientations with the aid of normals so that permittivities are evaluated based on the correct polarization.

3) Permittivity Estimation: The permittivity estimation for the points on a reflecting surface is based on solving the inverse reflection problem. The magnitude of the Fresnel reflection coefficient $|\Gamma|$ is calculated from the measured gain of multipath, ρ_n. The free-space path gain of a reflected multipath is given by

$$\mathrm{PG}_{\rm FS} = G_{\rm Tx} G_{\rm Rx}\left(\frac{\lambda}{4\pi d_{\rm r}}\right)^2, \tag{9}$$

where reflection point on a surface is selected so that $d_{\rm r}$ is the shortest path. Taking the ratio of (1) and (9) and solving for the reflection coefficient yields the magnitude of reflection coefficient as,

$$|\Gamma| = \sqrt{\frac{\rm PG}{\rm PG_{FS}}}. \tag{10}$$

It is noteworthy to mention that only magnitude of the reflection coefficient is considered because it is difficult to estimate their phase accurately due to inaccuracies of the complex antenna radiation pattern and antenna location estimates in the channel sounding. Also, estimating the real part of the complex permittivity is more substantial as the magnitude of its imaginary part is typically much smaller than the real part. From geometrical optics, the Fresnel reflection coefficients are given by relative permittivity ϵ_r of a reflecting surface and wave incidence angle α as

$$\Gamma_{\perp} = \frac{\cos\alpha - \sqrt{\epsilon_{\rm r} - \sin^2\alpha}}{\cos\alpha + \sqrt{\epsilon_r - \sin^2\alpha}}, \tag{11}$$

$$\Gamma_{\parallel} = \frac{-\epsilon_{\rm r}\cos\alpha + \sqrt{\epsilon_{\rm r} - \sin^2\alpha}}{\epsilon_{\rm r}\cos\alpha + \sqrt{\epsilon_{\rm r} - \sin^2\alpha}}. \tag{12}$$

The expressions (11) and (12) are valid when the first medium is air ($\epsilon_{\rm r} = 1$, $\mu_{\rm r} = 1$) and the second medium is a dielectric [14], [39]. The reflection coefficient in (11) is always negative, while in case of (12), the reflection coefficient is negative for incident angles smaller than the Brewster angle and it is positive for incident angles greater than the Brewster angle. Re-arranging (11) and (12) and solving these for the permittivity yields

$$\epsilon_{\rm r}(\Gamma_{\perp}, \alpha) = \cos^2\alpha\left[\frac{1 - \Gamma_{\perp}}{1 + \Gamma_{\perp}}\right]^2 + \sin^2\alpha, \tag{13}$$

[1] $\delta_{\rm plane} < \delta_{\rm max} = \dfrac{\lambda}{8\cos\alpha}$, where α is the incident angle of the ray-path.

0018-926X (c) 2018 IEEE. Personal use is permitted, but republication/redistribution requires IEEE permission. See http://www.ieee.org/publications_standards/publications/rights/index.html for more information.

This article has been accepted for publication in a future issue of this journal, but has not been fully edited. Content may change prior to final publication. Citation information: DOI 10.1109/TAP.2018.2829798, IEEE Transactions on Antennas and Propagation

$$\epsilon_{\mathrm{r}}(\Gamma_{\|},\alpha) = \frac{1}{2\cos^2\alpha}\cdot\left[\frac{1-\Gamma_{\|}}{1+\Gamma_{\|}}\right]^2 \cdot \left\{1+\frac{\sqrt{(1-\Gamma_{\|})^2-4\cos^2\alpha\sin^2\alpha(1+\Gamma_{\|})^2}}{(1-\Gamma_{\|})}\right\}. \tag{14}$$

The permittivity corresponding to each point on the reflecting surface is calculated using (13) and (14) for vertically and horizontally oriented reflecting surfaces[2], respectively. It is important to note that (13) and (14) are invalid for $\Gamma = -1$, whereas (14) is also invalid for the grazing incidence ($\alpha = \pi/2$). For $|\Gamma| \to 1$ in (10), (13) and (14) result in large permittivity values representing the metal surfaces. Since we only have the magnitude of the reflection coefficient available from (10), allocating an appropriate sign to the reflection coefficient allows us to correctly estimate the permittivity of the reflecting surface through (13) and (14). Hence, the reflections coefficients corresponding to the two polarizations in the permittivity range between 1 to 100 are determined as

$$\Gamma_{\perp} = -|\Gamma|,$$
$$\Gamma_{\|} = \begin{cases} -|\Gamma|, & 0 \le \alpha \le \alpha_{\mathrm{B}}^{\epsilon_{\mathrm{r}}=1} \\ +|\Gamma|, & \alpha_{\mathrm{B}}^{\epsilon_{\mathrm{r}}=100} \le \alpha \le \pi/2 \end{cases}, \tag{15}$$

where $\alpha_{\mathrm{B}}^{\epsilon_{\mathrm{r}}}$ is the Brewster angle corresponding to the permittivity ϵ_{r}. The sign of the reflection coefficient is indeterminable within the region bounded by the permittivity curve for $\alpha_{\mathrm{B}}^{\epsilon_{\mathrm{r}}=1} \le \alpha \le \alpha_{\mathrm{B}}^{\epsilon_{\mathrm{r}}=100}$, with $\alpha_{\mathrm{B}}^{\epsilon_{\mathrm{r}}=1} = 51°$ and $\alpha_{\mathrm{B}}^{\epsilon_{\mathrm{r}}=100} = 84.3°$. We call this as the ambiguity region for reflection coefficient. The most affected range of $\alpha_{\mathrm{B}}^{\epsilon_{\mathrm{r}}}$ is $70° - 80°$, where there is a risk of maximum 40% ambiguity. However, practically, this is not a serious drawback of the proposed method as the channel sounding is usually performed for multiple links. In the channel sounding, a surface may produce specular reflections corresponding to multiple links with varying incident and reflecting angles. It may be possible that one of these links have a reflection from the surface that falls into the ambiguity region, but other links may not have the same problem. When calculating the permittivity of a surface, we choose a median value of reflection coefficients from different links in order to reduce the impact of ambiguous estimates. The more number of links covered in the channel sounding, the less likely it is that a reflecting surface suffers from ambiguous permittivity estimates.

III. Millimeter Wave Radio Channel Sounding and Multipath Detection

The on-site permittivity estimation method described in Section II is substantiated by radio channel measurements at 60 GHz in a large empty office. We chose the experimental setup such that it meets the conditions for the effective use of the proposed permittivity estimation method, defined in Section II-A; the high radio frequency of the measurements and few link-blocking and scattering objects in the office provide us with abundant single-bounce reflections for a

[2]It is possible to determine the permittivity for skewed or slanted surfaces, please see the appendix for further details.

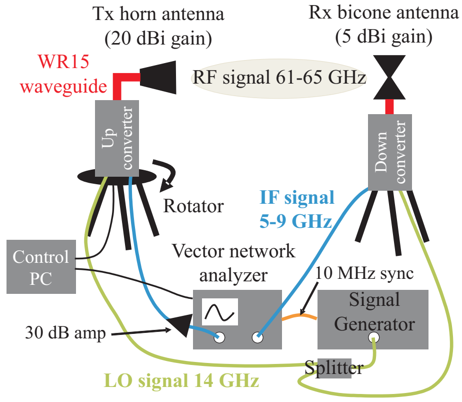

Fig. 3. Schematic of the radio channel sounder.

comprehensive estimation of the permittivity of materials constituting the environment. The point cloud of the office was obtained in conjunction with this measurement using a laser scanner [40]. The following subsections provide a brief overview of the measurements and the subsequent multipath parameter estimation process.

A. Experimental Setup and Channel Sounding

The radio channel sounding was performed using the setup illustrated in Fig. 3. Vector network analyzer (VNA) is the core data acquisition component of the setup that allows delay- and phase-synchronized measurements of transfer functions over wide bandwidths of radio channels. The VNA used in this channel sounder setup allows us to obtain absolute phase change due to the device under test, i.e., the radio channel in our case. The intermediate frequency (IF) signals from the VNA are mixed with those of a local oscillator (LO) using frequency up- and down-converters. The IF signal at the VNA is swept from 4 to 8 GHz, while LO supplies a 16.5 GHz continuous wave signal, resulting in the radio frequency (RF) range from 61 to 65 GHz. The 4 GHz bandwidth allows a fine delay resolution of 0.25 ns. The phase of the LO signal is locked to the VNA using a 10 MHz reference signal from the VNA. The Tx and Rx antennas are a standard gain horn and a bicone, respectively. The bicone is omnidirectional on the azimuth plane with maximum 5 dBi gain, while it covers only a narrow range of the elevation angle with 11° half power beamwidth. The horn antenna has 20 dBi gain with about 18° half power beamwidth both on the azimuth and elevation domains and with 35 dB cross-polarization discrimination. This measurement setup provides the effective isotropic radiated power (EIRP) of 30 dBm and allows the maximum measurable pathloss of 130 dB. Angular characteristics of radio channels can be measured by rotating the Tx horn antenna using an electromechanical rotator. The measurements were accomplished with the azimuthal scan of 360° using a 1° step; the elevation scan was not considered. In the measurements, we only considered vertical-to-vertical (VV) polarization configuration of the Tx and Rx antennas.

The sounding site is a large and empty modern office room with an approximate dimension of $18\times22\times3$ m^3 as depicted in

0018-926X (c) 2018 IEEE. Personal use is permitted, but republication/redistribution requires IEEE permission. See http://www.ieee.org/publications_standards/publications/rights/index.html for more information.

This article has been accepted for publication in a future issue of this journal, but has not been fully edited. Content may change prior to final publication. Citation information: DOI 10.1109/TAP.2018.2829798, IEEE Transactions on Antennas and Propagation

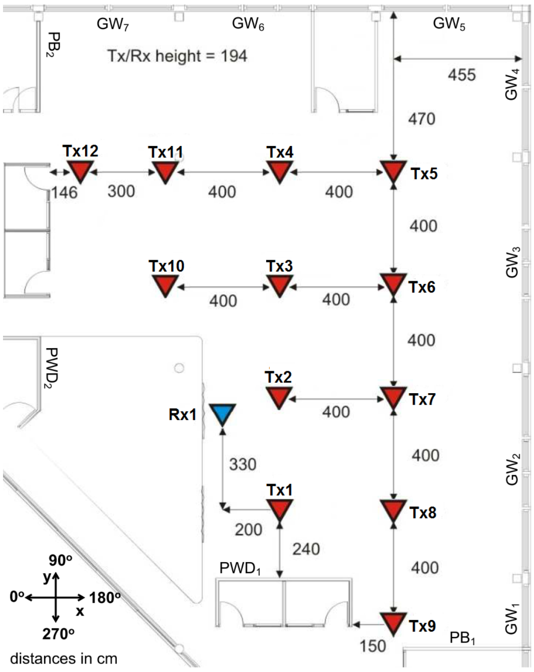

Fig. 4. Layout of the measurement site specifying positions of the Tx and Rx antennas, plasterboard (PB_x) walls, plywood (PWD_x) walls and glass windows (GW_x); where x is the index number.

Fig. 4. The figure includes setups of 12 Tx-Rx links, measured with a single Tx position and 12 Rx positions. The Tx and Rx antenna heights were kept fixed at 194 cm. To ensure static radio channels during antenna scanning and frequency sweeps of the VNA, human activity in the room was restricted.

B. Multidimensional Multipath Detection

A set of multipaths are estimated from the 60 GHz radio channel measurements based on the local maxima search in the power angular-delay profile (PADP); the local maxima are considered as the candidates of the paths reflected off the flat and electrically large surfaces in the room. For each Tx-Rx link, a PADP is calculated by taking the inverse discrete Fourier transform of the channel transfer function $H(\phi_i, f_j)$ over pointing angles of the Tx horn antenna ϕ_i and frequency samples f_j; where $1 \leq i \leq 360$ are the indices of the pointing angles in the range from $0°-359°$ and $1 \leq j \leq 2001$ are the indices of the frequency samples in the range from 61–65 GHz, respectively. The multipath detection consists of local maxima search in the PADP above the noise level, providing their coarse estimation of the power, delay and azimuth AoD. Specifically, for a single pointing angle of the Tx horn antenna, the local maxima are defined as peaks in the channel impulse response (CIR). The powers of the peaks are at least ΔP_{mean} greater than the local mean of the CIR over a sliding delay-window τ_{w}. In this analysis, τ_{w} and ΔP_{mean} are heuristically determined as 1.25 ns and 5 dB, respectively. Fine estimates of the power, delay and the azimuth AoD of each multipath are then obtained by matching the shape of the PADP around the coarsely detected peaks with those from band- and angular-limited power profiles, given by the sinc-function and the main beam pattern of the Tx horn antenna, respectively [41]. To

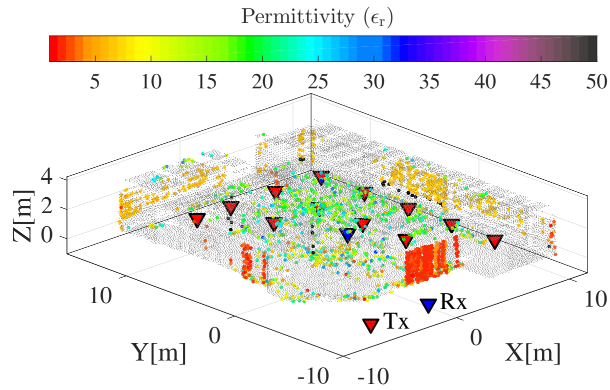

Fig. 5. Unclassified permittivity map visualizing reflecting surfaces colored with estimated permittivity values.

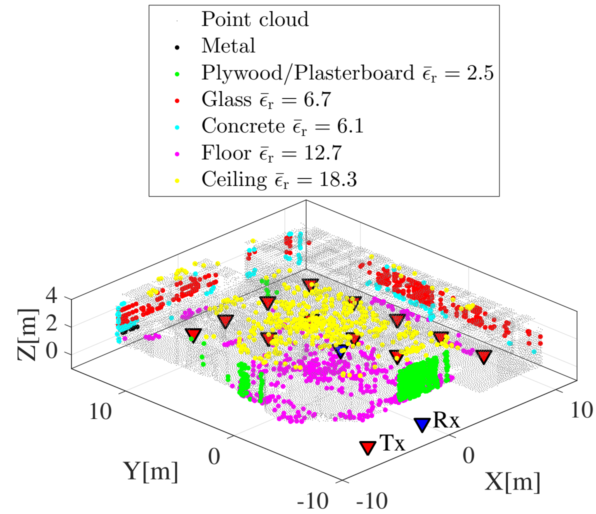

Fig. 6. Classified permittivity map visualizing reflecting surfaces colored with mean permittivities.

obtain the propagation path gain, the combined Tx-Rx antenna gain is de-embedded from the measured path gain estimate with the assumption that the path arrives in the horizontal two-dimensional (2D) plane, i.e., $\psi^{\mathrm{Tx}} = 0°$, which is due to the limited configuration of the channel sounder where only azimuth AoD is available, as described in the Section III-A. For further details on this method, the readers are referred to [42] and the references therein. Only a limited subset of multipath parameters defined in (2) are available from the present channel sounding as denoted by

$$\mathcal{P}_{\mathrm{M}}^{(l)} = \{\rho_n^{\mathrm{VV}}, \tau_n, \phi_n^{\mathrm{Tx}}\}_{n=1}^{N_l}, \tag{16}$$

where ρ_n^{VV}, τ_n, ϕ_n^{Tx} is the path gain for VV polarization of the Tx and Rx fields, delay, and azimuth AoD of the n-th path, respectively, with total N_l number of paths in the l-th Tx-Rx link.

IV. 3D Permittivity Map

The method proposed for permittivity estimation in Section II is implemented using MATLAB. The method is applied to the point cloud and multipaths from the empty office

0018-926X (c) 2018 IEEE. Personal use is permitted, but republication/redistribution requires IEEE permission. See http://www.ieee.org/publications_standards/publications/rights/index.html for more information.

This article has been accepted for publication in a future issue of this journal, but has not been fully edited. Content may change prior to final publication. Citation information: DOI 10.1109/TAP.2018.2829798, IEEE Transactions on Antennas and Propagation

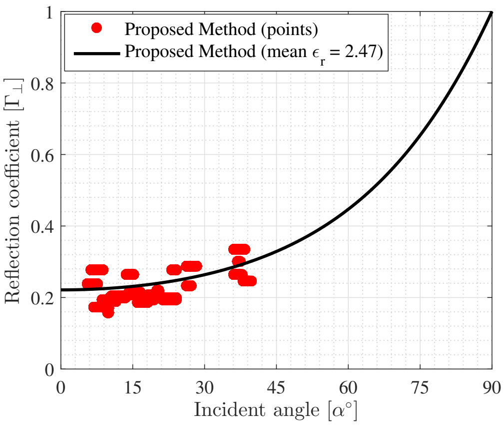

Fig. 7. Comparison of theoretical and estimated magnitude of the reflection coefficients $|\Gamma_\perp|$ for the plywood wall (PWD_1).

measurements described in the Section III. For the point cloud employed in this study, the position accuracy of each point acquired through the laser scanner is in the order of 5 mm. The reflecting surfaces are identified and their permittivity ϵ_r is estimated. It is found in this analysis that the reflecting surfaces at the measurement site can be considered horizontal or vertical, and that all the identified surfaces are flat and large-enough compared to the first Fresnel zones of the multipaths. With the available point cloud density of the empty office, $\gamma_{\mathrm{th}} = 1°$ and $\delta_{\mathrm{max}} = 5\,\mathrm{mm}$ are used as specular reflection and maximum allowable surface roughness, respectively. Other factors that influence the choice of a suitable value for δ_{max} are the laser scanning accuracy and the operating frequency. Since the combined Tx-Rx antenna gain is compensated from the measured specular multipaths only in 2D as described in the Section III-B, this causes an uncertainty in the permittivity estimation which is more profound for reflecting surfaces on the ceiling and floor. With the aid of delay and azimuth AoD of the multipath reflecting off the ceiling and floor, they can be easily distinguished from each other during specular multipath matching process. In summary, the measurements and data-processing uncertainties results a variability of $1-3$ dB in the magnitude of reflection coefficient corresponding to the points on the reflecting surfaces, which is then translated to the estimated permittivity. This can be more intuitively explained with Fig. 7 that illustrates the relationship between the magnitude of reflection coefficient $|\Gamma|$ and incident angle α. The dots in the figure represent Fresnel reflection coefficient estimates from the proposed method for the plywood wall (PWD_1), while the line shows Fresnel reflection coefficients with the estimated permittivity of the same wall. For this wall, the range of incident angle is limited to $0° - 45°$. The estimated magnitude of reflection coefficient follows the theoretical curve with the estimated mean permittivity of the same wall.

A. Unclassified Map

The point cloud colored with the estimated permittivity is visualized in Fig. 5, and is referred to as an unclassified map hereinafter. Not all the points are colored because reflections were not observed from them in the measurements; they are left undesignated and colored in gray. We have used 60 multipaths per Tx-Rx link on average to color the point cloud. The estimated ϵ_r values vary slightly over each reflecting surface partly due to the measurement uncertainty. However, this variation remains less than 2 in terms of the standard deviation for the estimated ϵ_r of each surface. This variation is due to the fact that all the points on a reflecting surface that meet (8) for a particular link are assigned with the same estimate of the reflection coefficient, whereas, the estimate comes from only one sample point on the surface. $\phi_{\mathrm{th}} = 1°$ and $\tau_{\mathrm{th}} = 2\,\mathrm{ns}$ are used as the optimal values of the threshold margins for matching measured and simulated multipaths according to the criteria given by (8). We manually try several combinations of different values for the threshold margins and consider the optimal combination as the one that has minimum values and allows maximum matching of measured and ray-traced paths at the same time. A single set of threshold margins are used for all the surfaces in the environment. In principle, the number of colored points in Fig. 5 increases by allowing more threshold margins and detecting more reflecting surfaces, but at the cost of more variation of the permittivity estimates. Our case demonstrated that measuring only 12 Tx-Rx links allowed the permittivity estimates as comprehensive as Fig. 5. A few exemplary surfaces identified in the considered environment are individually illustrated in Fig. 8(a-d) overlaying the raw estimated permittivity ϵ_r values. Despite the fact that only azimuth AoD (ϕ) is available from measurements, the comparison of propagation delay (τ) of measured and ray-traced paths allows us to obtain more than one specular reflection point on these reflecting surfaces. Figure 8(a-b) depicts plywood wall partitions with a blue and orange decorative paints, respectively. The estimated permittivity values, ϵ_r, ranging between $1.5 - 4.5$ are overlaid, with the mean value of 2.5. Figure 8(c) represents glass windows with ϵ_r varying within $5.5 - 8$ and with the mean of 6.7. Figure 8(d) shows metal heaters below glass windows as effective reflectors. Since they are not dielectric materials, their estimated ϵ_r are much greater than other surfaces in the environment and are around 30 on average.

B. Classified Map

By applying a heuristic clustering method to points according to their permittivity estimates, the reflecting surfaces are classified into their constituent materials. In this heuristic clustering method, the neighboring reflecting points with similar permittivity estimates are grouped together, and the material of the reflecting surface constituting these points and their mean permittivity are compared with the physical material evidence and the values available in the ITU recommendation [14], respectively. The mean permittivity of a reflecting surface is obtained by averaging the raw permittivity estimates of all the points on the surface, which also averages out the uncertainties in these estimates. The 3D permittivity map with the material and permittivity classification is illustrated in the Fig. 6. The classified mean permittivity values are tabulated in Table II, along with their physical evidence and corresponding values

0018-926X (c) 2018 IEEE. Personal use is permitted, but republication/redistribution requires IEEE permission. See http://www.ieee.org/publications_standards/publications/rights/index.html for more information.

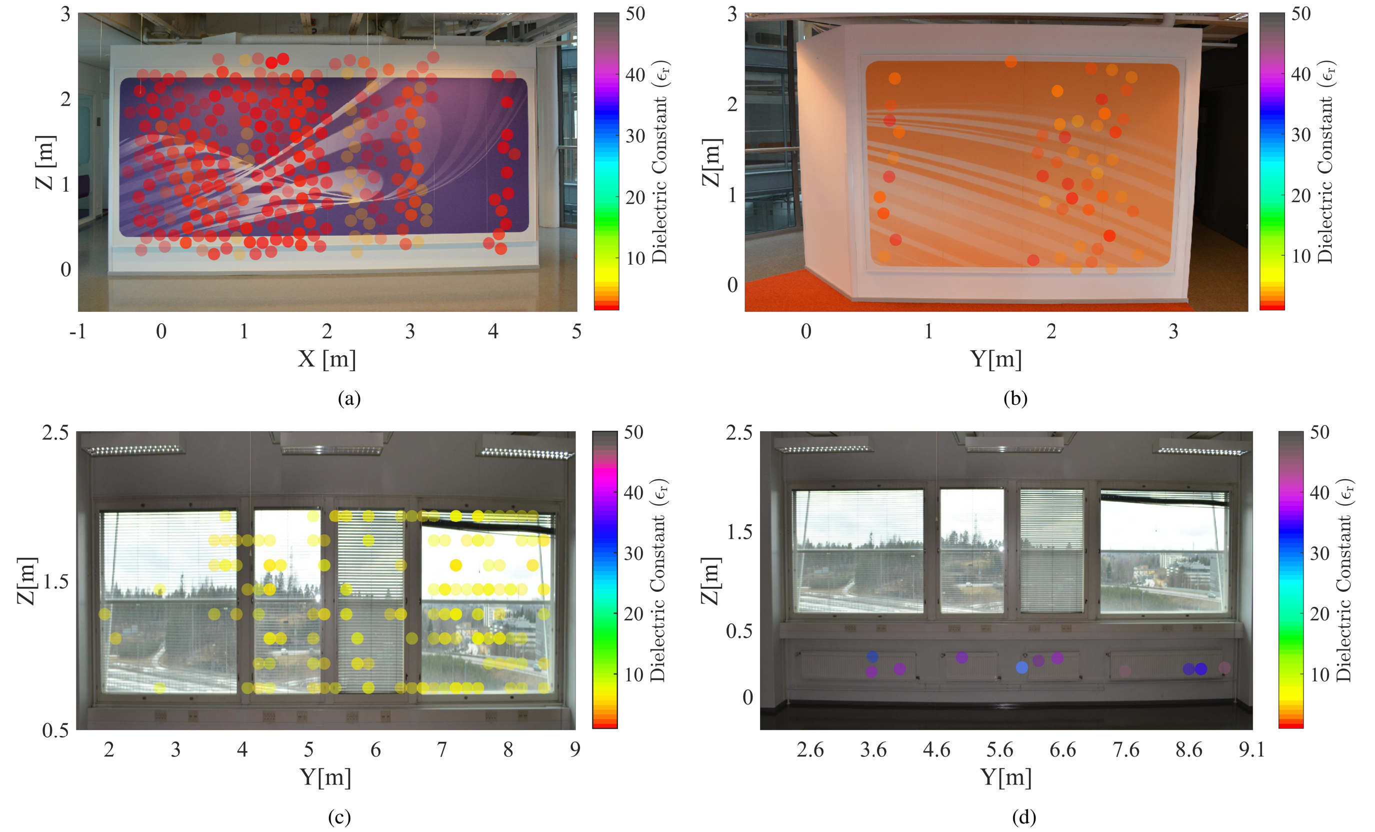

Fig. 8. Identified scatterer overlaying estimated permittivity (ϵ_r) from point cloud (a)-(b) plywood wall (PWD_1 and PWD_2 in Fig. 4), (c) glass window (GW_2 in Fig. 4), and (d) metal heaters.[3]

TABLE II
MEAN ESTIMATED PERMITTIVITY, $\bar{\epsilon}_r$, AND IDENTIFIED MATERIAL OF SURFACES WITH ITU-R VALUES.

Mean estimated $\bar{\epsilon}_r$	**ITU-R contender** ϵ_r	**Classified material**
2.6	2.9	Plasterboard
2.5	2.4	Plywood
6.7	6.27	Glass
6.1	5.31	Concrete
12.7	–	Floor (NI)
18.3	–	Ceiling (NI)
>20	–	Metal

in the ITU-R recommendation. The floor and ceiling material could not be identified accurately, and hence, are marked with the label *not identified* (NI). The estimated mean permittivity values of the classified materials are consistent with the ITU-R values according to Table II, thus showing the validity of our method. For ease in visualization, the panoramic view of the environment is presented in Fig. 9, highlighting the identified regions of reflections with mean permittivity, $\bar{\epsilon}_r$. The figure illustrates the southern and the northern half of the environment, respectively, which includes plywood and plasterboard walls, glass windows, and metal heater surfaces.

V. Conclusion

This paper presented a novel method for on-site permittivity estimation of different materials in built environments. The method identifies reflecting surfaces and solves the inverse reflection problem from a limited set of multipath channel sounding. Two conditions are identified to guarantee the proper functioning of the proposed method, i.e., availability of accurate geometrical database of the environment and dominance of single-bounce reflection in radio propagation. The proposed method is experimentally verified at 60 GHz in a large empty office room where the mentioned two conditions are satisfactorily met. The method performs matching of measured multipaths with those from ray-tracing using the accurate point cloud description of the given environment. The reflecting surfaces are classified according to the estimated permittivity, yielding consistent observations with physical material evidence and values presented in the ITU recommendation. The estimated permittivity values and subsequent material classification are visualized as a 3D map by coloring the point cloud of the environment, giving an intuitive understanding of material dielectric properties. It has been successfully demonstrated that dielectric properties can be characterized on-site using a limited set of channel sounding campaign, without conducting isolated measurements of the composite materials in an anechoic chamber or in-situ measurements of built environments. The evaluated permittivity map plays a crucial role in site-specific radio wave propagation simulations intended for 5G small-cell coverage study.

[3]During the measurements campaign, the window blinds were cleared off.

0018-926X (c) 2018 IEEE. Personal use is permitted, but republication/redistribution requires IEEE permission. See http://www.ieee.org/publications_standards/publications/rights/index.html for more information.

This article has been accepted for publication in a future issue of this journal, but has not been fully edited. Content may change prior to final publication. Citation information: DOI 10.1109/TAP.2018.2829798, IEEE Transactions on Antennas and Propagation

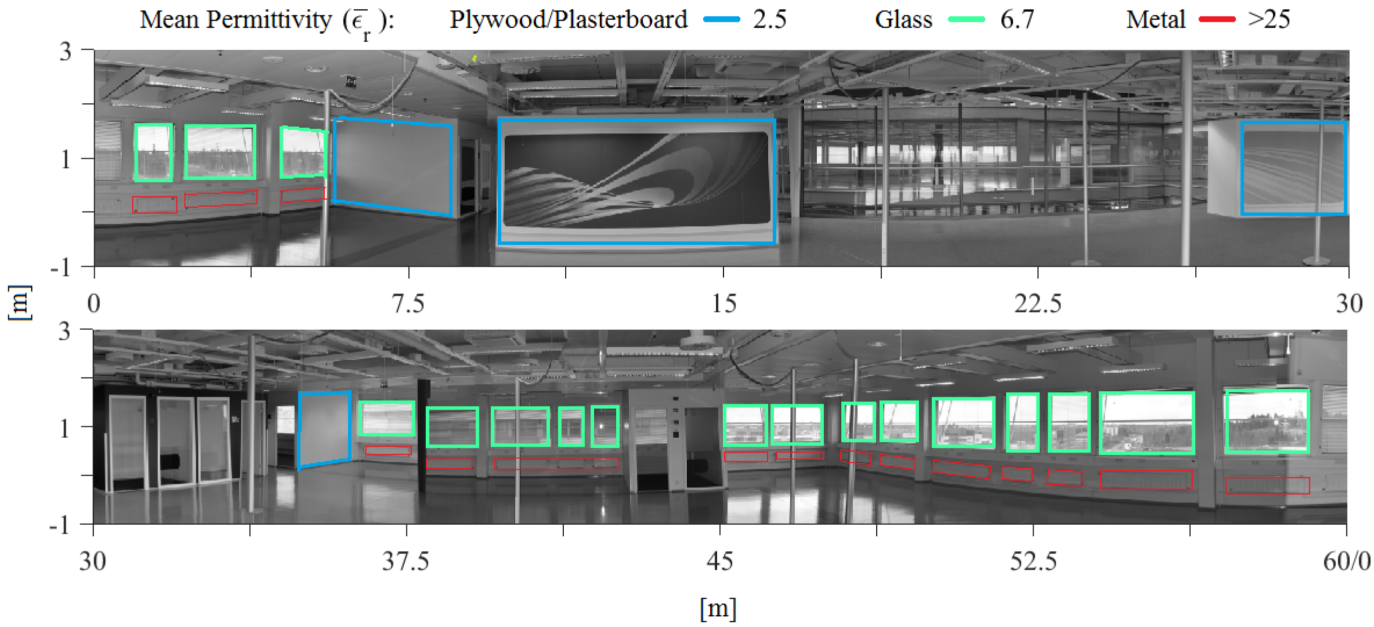

Fig. 9. Panoramic view of the measurement environment highlighting the identified scatterer regions with mean permittivity.

Appendix

For a a skewed or slanted surface, the permittivity is evaluated in combination of (13) and (14) since the incident field to the surface contain both parallel and perpendicular component. The electric field at the Tx antenna is transformed from spherical to the cartesian coordinate system. The electric field $\boldsymbol{E}_\mathrm{i}$ incident onto a reflecting surface is decomposed into its parallel $E_\mathrm{i}^{\|}$ and perpendicular $E_\mathrm{i}^{\perp}$ components according to the local coordinate system of the surface as

$$\begin{gathered}\boldsymbol{E}_\mathrm{i} = E_\mathrm{i}^{\|}\boldsymbol{u}_{\|} + E_\mathrm{i}^{\perp}\boldsymbol{u}_{\perp}, \\ \boldsymbol{u}_{\perp} = \frac{\boldsymbol{n}\times\boldsymbol{k}_\mathrm{i}}{\|\boldsymbol{n}\times\boldsymbol{k}_\mathrm{i}\|}, \quad \boldsymbol{u}_{\|} = \frac{\boldsymbol{k}_\mathrm{i}\times\boldsymbol{u}_{\perp}}{\|\boldsymbol{k}_\mathrm{i}\times\boldsymbol{u}_{\perp}\|},\end{gathered} \tag{17}$$

where $\boldsymbol{u}_{\|}$ and $\boldsymbol{u}_{\perp}$ are the unit vectors of the parallel and perpendicular polarizations for the slanted surface, respectively, and $\boldsymbol{n}$ and $\boldsymbol{k}_\mathrm{i}$ refers to the surface normal and propagation vector of the incident field, all defined on the global coordinate system. Thus, the total electric field reflected off the slanted surface is

$$\begin{gathered}\boldsymbol{E}_\mathrm{r} = \Gamma_{\|}E_\mathrm{i}^{\|}\boldsymbol{u}'_{\|} + \Gamma_{\perp}E_\mathrm{i}^{\perp}\boldsymbol{u}'_{\perp}, \\ \boldsymbol{u}'_{\perp} = \frac{\boldsymbol{n}\times\boldsymbol{k}_\mathrm{r}}{\|\boldsymbol{n}\times\boldsymbol{k}_\mathrm{r}\|}, \quad \boldsymbol{u}'_{\|} = -\frac{\boldsymbol{k}_\mathrm{r}\times\boldsymbol{u}'_{\perp}}{\|\boldsymbol{k}_\mathrm{r}\times\boldsymbol{u}'_{\perp}\|}.\end{gathered} \tag{18}$$

The unit vectors, $\boldsymbol{u}'_{\|}$ and $\boldsymbol{u}'_{\perp}$, specify the direction of parallel and perpendicular components of $\boldsymbol{E}_\mathrm{r}$, respectively and $\boldsymbol{k}_\mathrm{r}$ is its propagation vector. The electric field at the Rx antenna is derived by transforming $\boldsymbol{E}_\mathrm{r}$ from cartesian to antenna's spherical coordinate system, multiplied with the free space green's function. When dual-polarized field measurements and/or reflection measurements from a slanted surface are available, the permittivity of the surface is estimated by minimizing the difference between empirical and theoretical magnitude of the reflection coefficients for the two polarizations, denoted as Γ_emp and Γ_theo, respectively. The minimizing function is formulated as,

$$\mathcal{G}(\epsilon_\mathrm{r}) = (|\Gamma_\mathrm{emp}^{\|}| - |\Gamma_\mathrm{theo}^{\|}|)^2 + (|\Gamma_\mathrm{emp}^{\perp}| - |\Gamma_\mathrm{theo}^{\perp}|)^2. \tag{19}$$

Acknowledgment

The authors would like to thank Dr. Mikko Kyrö, Dr. Jan Järveläinen and Dr. Yang Miao for their assistance in the measurements campaign. The authors are also grateful to Dr. Aki Karttunen for his useful comments.

References

[1] A. Ghosh, T. A. Thomas, M. C. Cudak, R. Ratasuk, P. Moorut, F. W. Vook, T. S. Rappaport, G. R. MacCartney, S. Sun, and S. Nie, "Millimeter-wave enhanced local area systems: A high-data-rate approach for future wireless networks," *IEEE J. Sel. Areas Commun.*, vol. 32, no. 6, pp. 1152–1163, June 2014.

[2] T. S. Rappaport, S. Sun, R. Mayzus, H. Zhao, Y. Azar, K. Wang, G. Wong, J. K. Schulz, M. Samimi, and F. Gutierrez, "Millimeter wave mobile communications for 5G cellular: It will work!" *IEEE Access*, vol. 1, pp. 335–349, May 2013.

[3] A. Valcarce, G. D. L. Roche, A. Jüttner, D. Lopez-Peŕez, and J. Zhang, "Applying FDTD to the coverage prediction of wimax femtocells," *EURASIP J. Wireless Commun. Netw.*, vol. 1, Mar. 2009.

[4] L. Nagy, "Comparison and application of FDTD and ray optical method for indoor wave propagation modeling," in *Proc. 4th European Conf. Antennas Propag. (EuCAP'10)*, Barcelona, Spain, Apr. 2010.

[5] A. C. M. Austin, M. J. Neve, and G. B. Rowe, "Modeling propagation in multifloor buildings using the FDTD method," *IEEE Trans. Antennas Propag.*, vol. 59, no. 11, pp. 4239–4246, Nov. 2011.

[6] U. T. Virk, K. Haneda, V. M. Kolmonen, J. F. Wagen, and P. Vainikainen, "Full-wave characterization of indoor office environment for accurate coverage analysis," in *Proc. Int. Conf. Electromagn. Adv. Applicat. (ICEAA'13)*, Turin, Italy, Sep. 2013, pp. 1197–1200.

[7] T. Fugen, J. Maurer, T. Kayser, and W. Wiesbeck, "Capability of 3-D ray tracing for defining parameter sets for the specification of future mobile communications systems," *IEEE Trans. Antennas Propag.*, vol. 54, no. 11, pp. 3125–3137, Nov. 2006.

[8] M. Peter, W. Keusgen, and R. Felbecker, "Measurement and ray-tracing simulation of the 60 GHz indoor broadband channel: Model accuracy and parameterization," in *Proc. 2nd European Conf. Antennas Propag. (EuCAP'07)*, Edinburgh, Uk, Nov. 2007.

0018-926X (c) 2018 IEEE. Personal use is permitted, but republication/redistribution requires IEEE permission. See http://www.ieee.org/publications_standards/publications/rights/index.html for more information.

This article has been accepted for publication in a future issue of this journal, but has not been fully edited. Content may change prior to final publication. Citation information: DOI 10.1109/TAP.2018.2829798, IEEE Transactions on Antennas and Propagation

[9] V. Degli-Esposti, F. Fuschini, E. M. Vitucci, M. Barbiroli, M. Zoli, L. Tian, X. Yin, D. A. Dupleich, R. Müller, C. Schneider, and R. S. Thomä, "Ray-tracing-based mm-wave beamforming assessment," *IEEE Access*, vol. 2, pp. 1314–1325, Oct. 2014.

[10] J. Pascual-García, J. M. Molina-García-Pardo, M. T. Martínez-Inglés, J. V. Rodrguez, and N. Saurín-Serrano, "On the importance of diffuse scattering model parameterization in indoor wireless channels at mm-wave frequencies," *IEEE Access*, vol. 4, pp. 688–701, Feb. 2016.

[11] B. Peng, S. Rey, and T. Kürner, "Channel characteristics study for future indoor millimeter and submillimeter wireless communications," in *Proc. 10th European Conf. Antennas Propag. (EuCAP'16)*, Davos, Switzerland, Apr. 2016.

[12] J. Järveläinen, K. Haneda, and A. Karttunen, "Indoor propagation channel simulations at 60 GHz using point cloud data," *IEEE Trans. Antennas Propag.*, vol. 64, no. 10, pp. 4457–4467, Oct. 2016.

[13] J. Järveläinen, S. L. H. Nguyen, K. Haneda, R. Naderpour, and U. T. Virk, "Evaluation of millimeter-wave line-of-sight probability with point cloud data," *IEEE Wireless Commun. Lett.*, vol. 5, no. 3, pp. 228–231, June 2016.

[14] ITU-T, "Effect of building material and structures on radiowave propagation above about 100 MHz," International Telecommunication Union, Recommendation ITU-R P.2040-1, 2015.

[15] J. Lu, D. Steinbach, P. Cabrol, P. Pietraski, and R. V. Pragada, "Propagation characterization of an office building in the 60 GHz band," in *Proc. 8th European Conf. Antennas Propag. (EuCAP'14)*, The Hague, Netherlands, Apr. 2014.

[16] K. Sato, T. Manabe, T. Ihara, H. Saito, S. Ito, T. Tanaka, K. Sugai, N. Ohmi, Y. K. Y. Murakami, M. Shibayama, and T. Kimura, "Measurements of reflection and transmission characteristics of interior structures of office building in the 60-GHz band," *IEEE Trans. Antennas Propag.*, vol. 45, no. 12, pp. 1783–1792, Dec. 1997.

[17] J. Ahmadi-Shokouh, S. Noghanian, and H. Keshavarz, "Reflection coefficient measurement for north american house flooring at 57–64 GHz," *IEEE Antennas Wireless Propag. Lett.*, vol. 10, pp. 1321–1324, 2011.

[18] A. Hammoudeh, J. P. Pugliese, M. G. Sanchez, and E. Grindrod, "Comparison of reflection mechanisms from smooth and rough surfaces at 62 GHz," in *Proc. IEE Nat. Conf. Antennas Propag.*, York, UK, Apr. 1999, pp. 144–147.

[19] B. Langen, G. Lober, and W. Herzig, "Reflection and transmission behaviour of building materials at 60 GHz," in *Proc. 5th IEEE Int. Symp. Personal, Indoor and Mobile Radio Commun. (PIMRC'94)*, The Hague, Netherlands, Sep. 1994, pp. 505–509.

[20] I. Cuinas, J. P. Pugliese, A. Hammoudeh, and M. Sanchez, "Comparison of the electromagnetic properties of building materials at 5.8 GHz and 62.4 GHz," in *Proc. 52nd IEEE Veh. Tech. Conf. (VTC'00)*, vol. 2, Boston, MA, Sept. 2000, pp. 780–785.

[21] D. K. Ghodgaonkar, V. V. Varadan, and V. K. Varadan, "A free-space method for measurement of dielectric constants and loss tangents at microwave frequencies," *IEEE Trans. Instrum. Meas.*, vol. 38, no. 3, pp. 789–793, June 1989.

[22] Y. Huang and M. Nakhkash, "Characterisation of layered dielectric medium using reflection coefficient," *IET Electronics Lett.*, vol. 34, no. 12, pp. 1207–1208, June 1998.

[23] Z. Ma and S. Okamura, "Permittivity determination using amplitudes of transmission and reflection coefficients at microwave frequency," *IEEE Trans. Microw. Theory Techn.*, vol. 47, no. 5, pp. 546–550, May 1999.

[24] Z. Abbas, R. D. Pollard, and R. W. Kelsall, "Complex permittivity measurements at Ka-band using rectangular dielectric waveguide," *IEEE Trans. Instrum. Meas.*, vol. 50, no. 5, pp. 1334–1342, Oct. 2001.

[25] M. F. Akay, S. N. Kharkovsky, and U. C. Hasar, "An automated amplitudes-only measurement system for permittivity determination using free-space method," in *Proc. 18th IEEE Instrum. Meas. Tech. Conf. (IMTC'01)*, Budapest, Hungary, May 2001, pp. 503–506.

[26] Y. Shen, C. L. Law, and W. Dou, "Ultra-wideband measurement of the dielectric constant and loss tangent of concrete slabs," in *Proc. China-Japan Joint Microw. Conf.*, Shanghai, China, Sep. 2008, pp. 537–540.

[27] K. Haddadi and T. Lasri, "Geometrical optics-based model for dielectric constant and loss tangent free-space measurement," *IEEE Trans. Instrum. Meas.*, vol. 63, no. 7, pp. 1818–1823, July 2014.

[28] M. K. Olkkonen, V. Mikhnev, and E. Huuskonen-Snicker, "Complex permittivity of concrete in the frequency range 0.8 to 12 GHz," in *Proc. 7th European Conf. Antennas Propag. (EuCAP'13)*, Gothenburg, Sweden, Apr. 2013.

[29] C. D. Taylor, S. J. Gutierrez, S. L. Langdon, and K. L. Murphy, "On the propagation of RF into a building constructed of cinder block over the frequency range 200 MHz to 3 GHz," *IEEE Trans. Electromagn. Compat.*, vol. 41, no. 1, pp. 46–49, Feb. 1999.

[30] O. Landron, M. J. Feuerstein, and T. S. Rappaport, "A comparison of theoretical and empirical reflection coefficients for typical exterior wall surfaces in a mobile radio environment," *IEEE Trans. Antennas Propag.*, vol. 44, no. 3, pp. 341–351, Mar. 1996.

[31] M. Peter *et al.*, "Measurement results and final mmmagic channel models: Specular wall reflections and diffused scattering measurements," Millimetre-Wave Based Mobile Radio Access Network for Fifth Generation Integrated Communications (mmMAGIC), resreport H2020-ICT-671650-mmMAGIC/D2.2, May 2017. [Online]. Available: https://bscw.5g-mmmagic.eu/pub/bscw.cgi/d202656/mmMAGIC_D2-2.pdf

[32] L. M. Correia and P. O. Frances, "Estimation of materials characteristics from power measurements at 60 GHz," in *Proc. 5th IEEE Int. Symp. Personal, Indoor and Mobile Radio Commun.*, The Hague, Netherlands, Sep. 1994, pp. 510–513.

[33] I. Vilovic, N. Burum, and R. Nadj, "Estimation of dielectric constant of composite materials in buildings using reflected fields and PSO algorithm," in *Proc. 4th European Conf. Antennas Propag. (EuCAP'10)*, Barcelona, Spain, Apr. 2010.

[34] O. Landron, M. J. Feuerstein, and T. S. Rappaport, "In situ microwave reflection coefficient measurements for smooth and rough exterior wall surfaces," in *Proc. IEEE 43rd Veh. Techn. Conf. (VTC'93)*, Secaucus, NJ, May. 1993, pp. 77–80.

[35] B. Feitor, R. Caldeirinha, T. Fernandes, D. Ferreira, and N. Leonor, "Estimation of dielectric concrete properties from power measurements at 18.7 and 60 GHz," in *Proc. Loughborough Antennas Propag. Conf. (LAPC'11)*, Loughborough, UK, Nov. 2011.

[36] H. Bertoni, *Radio Propagation for Modern Wireless Systems*, ser. Wireless communications. Prentice Hall PTR, 2000.

[37] J. Järveläinen, "Measurement-based millimeter-wave radio channel simulations and modeling," Doctoral Dissertation, School of Electrical Engineering, Department of Radio Science and Engineering, Aalto University, Oct. 2016. [Online]. Available: https://aaltodoc.aalto.fi/handle/123456789/21931

[38] U. T. Virk, J. F. Wagen, and K. Haneda, "Simulating specular reflections for point cloud geometrical database of the environment," in *Proc. Loughborough Antennas Propag. Conf. (LAPC'15)*, Lougborough, UK, Nov. 2015.

[39] T. Rappaport, *Wireless Communications: Principles and Practice*, 2nd ed. Upper Saddle River, NJ, USA: Prentice Hall PTR, 2001.

[40] K. H. Thiel and A. Wehr, "Performance capabilities of laser-scanners- an overview and measurement principle analysis," *International Archives of Photogrammetry, Remote Sensing and Spatial Information Sciences*, vol. 36, no. 8/W2, pp. 14–18, 2004.

[41] K. Haneda, S. L. H. Nguyen, J. Järveläinen, and J. Putkonen, "Estimating the omni-directional pathloss from directional channel sounding," in *Proc. 10th European Conf. Antennas Propag. (EuCAP'16)*, Davos, Switzerland, Apr. 2016.

[42] S. L. H. Nguyen, K. Haneda, and J. Putkonen, "Dual-band multipath cluster analysis of small-cell backhaul channels in an urban street environment," in *Proc. IEEE Global Commun. Conf.*, Washington DC, Dec. 2016.

Usman Tahir Virk received the B.Sc. EE degree in electronics and telecommunications from University of Engineering and Technology, Lahore, Pakistan, in 2007. From 2007 to 2010, he was associated with the telecom industry in Pakistan as an O&M Engineer. He received the M.Sc. Tech. (Hons.) degree from Aalto University, Espoo, Finland in 2012, where he is pursuing his D.Sc. Tech degree in radio engineering. He is the recipient of Best Student Paper awards at the Loughborough Antennas and Propagation Conference (LAPC2015), Loughborough, United Kingdom and the 11th European Conference on Antennas and Propagation (EuCAP2017), Paris, France. He also received Nokia Foundation Scholarship 2017 in recognition of his doctoral research. He has been actively involved in research collaborations with other universities and industry for 5G radio channel modeling. His research interests include multi-band radio channel measurements, simulations and modeling focusing millimeter-wave (mm-Wave) frequencies for 5G systems and beyond, Radio Frequency (RF) and mm-Wave material characterization, massive MIMO, smart antennas, electromagnetic scattering problems, full-wave numerical techniques, and wireless communications for medical applications.

0018-926X (c) 2018 IEEE. Personal use is permitted, but republication/redistribution requires IEEE permission. See http://www.ieee.org/publications_standards/publications/rights/index.html for more information.

This article has been accepted for publication in a future issue of this journal, but has not been fully edited. Content may change prior to final publication. Citation information: DOI 10.1109/TAP.2018.2829798, IEEE Transactions on Antennas and Propagation

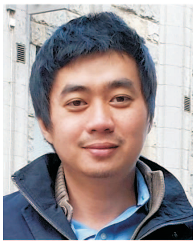

Sinh Le Hong Nguyen (S10, M13) received the B.Eng. degree in electronics and telecommunications engineering from Ho Chi Minh City University of Technology, Ho Chi Minh, Vietnam, in 2007, the M.Sc. degree in electrical engineering from Florida International University, Miami, USA in 2009, and the Ph.D. degree in electrical engineering from Concordia University, Montreal, Canada, in 2013. From 2013 to 2014, he was a Postdoctoral Fellow at McGill University, Canada. From 2014 to 2018, he was with Aalto University, Finland, as a Postdoctoral Researcher. Since 2018 he has been with Ericsson Research Sweden as a Senior Researcher. He has participated and actively contributed to several university-industry collaborative and EU H2020 projects on 5G technologies. His current research interests include design and analysis of physical layer algorithms for 5G wireless backhaul network, millimeter-wave and massive MIMO systems, radio channel simulations and modelling, wireless localization, and the Internet of Things.

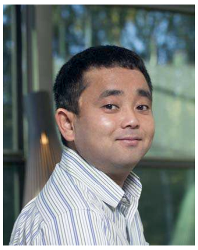

Katsuyuki Haneda (S03, M07) received the Doctor of Engineering from the Tokyo Institute of Technology, Tokyo, Japan, in 2007. Dr. Haneda is presently an associate professor in Aalto University School of Electrical Engineering. He is the recipient of the best paper award of the antennas and propagation track in the IEEE 77th Vehicular Technology Conference (VTC2013-Spring), Dresden, Germany, and of the best propagation paper award in the 7th European Conference on Antennas and Propagation (EuCAP2013), Gothenburg, Sweden. Dr. Haneda has been an associate editor of the IEEE Transactions on Antennas and Propagation between 2012 and 2016, and of an editor of the IEEE Transactions on Wireless Communications since 2013. He has also been an active member of a number of European COST Actions, e.g., CA15104 Inclusive Radio Communication Networks for 5G and beyond (IRACON), where he is a co-chair of a disciplinary working group on radio channels. His current research activity includes high-frequency radios such as millimeter-wave and beyond, wireless for medical, post-disaster scenarios and internet-of-things, and in-band full-duplex radio technologies.

Dr. Jean-Frédéric (Fred) Wagen is Professor at the HES-SO University of Applied Sciences and Arts - Western Switzerland in Fribourg. Since January 2000, he teaches computer network and telecommunication lectures. Prof. Wagen serves as Swiss Delegate for the COST IRACON and contributed to previous COST Actions since COST 231. Since receiving his diploma from EPFL in 1982, Fred Wagen achieved an MS. EE at Lehigh University and his PhD. EE at University of Illinois at Urbana-Champaign, USA. He then worked in the industry: 3 years at GTE Labs now Verizon (USA) and 9 years at Swisscom Innovations (Switzerland) in the areas of mobile radio communications: radio propagation, radio network planning, mobile systems, service deployment, and, in addition in academia, smartphone applications development and applied research projects recently related to propagation channel modeling and MANET. Dr. Wagen holds one patent.

0018-926X (c) 2018 IEEE. Personal use is permitted, but republication/redistribution requires IEEE permission. See http://www.ieee.org/publications_standards/publications/rights/index.html for more information.